Two-Dimensional Oxide Alloys Probed at the Atomic Level: (V,Fe)2O3 Honeycomb Monolayers on Pt(111)

P. Wemhoff, N. Nilius, C. Noguera, Jacek Goniakowski

Two-dimensional oxide alloys probed at the atomic level: $(V,Fe)_2O_3$ honeycomb monolayers on Pt(111)

P. I. Wemhoff,[†] N. Nilius,[*,†] C. Noguera,[‡] and J. Goniakowski[*,‡]

[†]*Institut für Physik, Carl von Ossietzky Universität,D-26111 Oldenburg, Germany*
[‡]*CNRS-Sorbonne Université, UMR 7588, INSP, F-75005 Paris, France*

E-mail: niklas.nilius@uni-oldenburg.de; jacek.goniakowski@insp.jussieu.fr

Abstract

While cation replacement has long been used to tailor the functionalities of oxide compounds, the growing industrial demand for nanoscale materials nowadays requires precise atomic scale characterization and understanding of the cation distribution. We report a successful synthesis and characterization of the two-dimensional $(V,Fe)_2O_3$ alloy supported on Pt(111) which is thermodynamically stable at realistic temperatures and for Fe contents up to 50%. Tight synergy between fine atomic resolution STM experiments and DFT calculations has revealed an unequivocal preference for formation of mixed V-Fe nearest-neighbor pairs, to a large extent driven by cation-cation electrostatic interactions. Moreover, Monte Carlo simulations have enabled an in-depth rationalization of the observed cation distribution in the honeycomb lattice. We show that the V-Fe mixing is restricted to 2D systems and not observed in the corresponding bulk systems, and that it is closely related to a change in vanadium oxidation state resulting from the interaction with the substrate. The flexibility of composition, of the distribution of cations and of their charge state provide levers to tune the properties of such two-dimensional oxide alloys and may thus enhance their potential for applications.

1 Introduction

While past efforts have mainly focused on metallic and semiconducting materials, the XXIth century technology has undoubtedly turned toward an intensified use of oxides.[1,2] However, whether for electronics applications, for superconducting devices, for MRAM memories, for catalysis, or for energy applications, binary oxides often do not display enough degrees of freedom to adjust their electronic, optical, magnetic or chemical response.

The physical and chemical versatility of oxides is largely expanded when moving from binary to ternary or even quaternary compounds,[3] as often encountered in nature where doping is the generality rather than the exception.[4] The controllable mixing of two oxides in a large range of compositions plays in modern materials science a role similar to that held by the alloying of metals, which, in the past, has allowed for unprecedented advances in the metallurgic industries.[5,6] Compositional changes in ternary oxides, for example, have been used to fine tune band gaps in order to produce materials for photovoltaic and photocatalytic applications.[7] Corporative effects of cations in perovskites, manganites, or ternary spinels are also present in the new materials for electronics, spintronics, or magnetism.[8–11] However, the field in which the impact of mixed oxides is the largest is undoubtedly that of heterogeneous

catalysis, where a wide range of chemical functionalities can be generated by altering the elemental composition.[12–15]

Despite this significance, the atomic-scale interrelation of lattice ions in a mixed oxide is not sufficiently understood to safely predict their combined response. Difficulties arise from the complex structural reorganization and charge compensation mechanisms upon replacing one lattice species by another. The insertion of cations with deviant valence, for example, entails reorganization of the oxygen network, while aliovalent anions may alter the charge state of their cationic neighbors.[16] Conditions for obtaining stable oxide solid solutions in a large composition range have been explored in bulk materials, and were found to be governed by the similarity of the parent atomic structures, of the ionic radii, and of the cation valences.[3,4,17–20]

Understanding characteristics at the atomic scale is of key importance for the nano-size materials demanded by modern industries. A large variety of novel phenomena and properties is expected in mixed nano-oxides, in close analogy to those recently discovered in metallic nanoalloys.[21] Recent examples of oxide nanoalloys include, among others, Ce-Ti,[22] Zn-Mg,[23] or Ti-Si[24] oxide nanoparticles, and thin oxide films based on the intermixing of Si-Al,[25] Si-Li,[26] Ti-Ba,[27,28] Mo-Ca[29] or two-dimensional (2D) transition metal oxide alloys with distinct honeycomb geometry.[30–33] Among them, particularly interesting and virtually unexplored cases concern those formed by oxides which do not mix in their bulk form. Their specific mixing behavior which is driven by the object size and/or dimensionality makes them artificial materials with no bulk equivalent, possibly associated to physico-chemical characteristics far beyond a mere average of those of their parents.

The present work addresses several of these issues. It reports the successful synthesis and characterization of a 2D oxide alloy, namely a $(V_{1-x}Fe_x)_2O_3$ monolayer (ML) supported on Pt(111), stable at realistic temperatures and in a large range of concentrations ($0 < x < 0.5$). Thanks to a combination of atomically resolved scanning tunnelling microscopy (STM) experiments, density functional theory (DFT) calculations and Monte Carlo (MC) simulations, it unravels the STM signatures of the two cations and accesses their electronic characteristics and the composition-dependent cation distribution in the honeycomb lattice. A dedicated analysis highlights the key role of low dimensionality and of the interaction with the metallic substrate. We show that, in this 2D alloy, the tendency for V-Fe mixing which is absent in the bulk is tightly linked to a change of cation oxidation states.

2 Experimental and theoretical methods

2.1 Experimental methods

The experiments have been performed in an ultra-high vacuum chamber (p $\approx$ 1*10^{-10} mbar), containing a liquid-nitrogen cooled STM plus standard surface-science tools for sample preparation and analysis. STM imaging was performed in the constant current mode with electrochemically etched Au tips. The Pt(111) single crystal was cleaned by repeated cycles of Ne^+ sputtering, O_2 annealing at 750 K and vacuum flashing to 1200 K until sharp (1 $\times$ 1) reflexes and wide, atomically flat terraces were observed in low-energy electron diffraction (LEED) and STM, respectively. Our preparation scheme for the mixed oxide layers comprised vacuum deposition of 0.05-0.3 ML of Fe followed by 0.3 ML V deposition in 1*10^{-6} mbar O_2, both performed at 550 K sample temperature. Crystallization into a honeycomb oxide was realized by vacuum annealing at 600 K for 10 min. The precise Fe/V ratio of so prepared honeycomb oxides was determined by counting the respective cations in several representative STM images that showed atomic scale contrast between Fe and V. We note that higher metal and O_2 exposure as well as different post-annealing conditions produced other mixed oxide configurations.

2.2 First principles simulations

DFT calculations were performed with the Vienna Ab-initio Simulation Package (VASP)[34,35] using the Projector Augmented Wave (PAW) method[36,37] to represent the electron-core interaction and a 400 eV energy cut-off in the development of Kohn-Sham orbitals on a plane-wave basis set. We have checked that an increase of the cut-off to 500 eV does not bring any noticeable modifications to the reported results. For example, for $VFeO_3$ and its parents Fe_2O_3 and V_2O_3, it changes the structure (film rumpling, anion-cation and cation-substrate bond lengths) by less than 0.01 Å, the electronic characteristics (anion, cation, and substrate charges) by less than 0.01 e per formula unit (f.u.) and the energetic behavior (formation energy of the mixed oxide) by less than 0.01 eV/f.u.

Dispersion-corrected exchange-correlation functional (optB88-vdW)[38–40] was employed, within the DFT+U approach proposed by Dudarev.[41,42] As in our previous studies,[20,32,43,44] we have used U values close to those reported in the literature: $U = 1.7$ eV for V, and $U = 3$ eV for Fe in the sesquioxides. We have checked that, with the present choice of U values, the DFT+U results are in close agreement with the more accurate HSE03 ones for selected configurations.[32,33] As a consequence, in the following, we will only report the DFT+U results.

All calculations were spin-polarized and the relative stability of non-magnetic (NM) and magnetic solutions with either parallel (FM) or anti-parallel (AF) spin moments was systematically tested. Ionic charges were estimated with the partition scheme proposed by Bader[45,46] and magnetic moments were obtained by integration of the spin density within the Bader's volumes. Simulations of STM images rely on the Tersoff-Hamann approximation[47] and atomic configurations were plotted with VESTA.[48]

We have considered Pt(111)-supported pure V_2O_3 and mixed $(V_{(1-x)}Fe_x)_2O_3$ ($0 < x < 0.5$) monolayers in an honeycomb structure on a (4×4)-Pt(111) unit cell, at the experimental bulk Pt lattice parameter (2.765 Å), Fig. 1 a. The sampling of the Brillouin zone was performed with the Γ-centered (4×4×1) Monkhorst-Pack mesh.[49] The Pt substrate was represented by a slab composed of four (111) atomic layers. We have checked that an increase of the metal thickness to 5 atomic layers yields negligible corrections on all reported quantities. The oxide film was deposited on one side of the metal slab and dipole correction was applied. All atomic coordinates of anions and cations as well as those of Pt atoms in the surface layer were allowed to fully relax until forces got lower than 0.01 eVÅ^{-1}. Remaining atoms of the metal substrate were relaxed in the direction normal to the surface only, except for the Pt atoms at the opposite slab surface which were kept fixed in bulk-like positions.

2.3 Monte Carlo simulations

In order to access the cation distribution in the monolayer at different compositions and at finite temperatures consistent with the experimental conditions, we have performed Monte Carlo simulations on the honeycomb lattice formed by the cationic sites. On this lattice, each cation has three first- (ortho-positions), six second- (meta-positions), and three third- (para-positions) cation neighbors, respectively, Fig. 1 b.

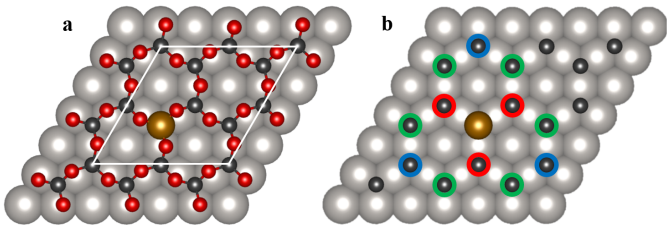

Figure 1: (a): honeycomb lattice with one Fe atom per (4 × 4)-Pt(111) unit cell. Black, golden, red, and gray balls represent V, Fe, O, and Pt atoms, respectively. (b): cation honeycomb lattice used in the MC simulations. The central golden cation has 3 first- (red), 6 second- (green) and 3 third- (blue) neighbors.

The effective interactions between cations on such a lattice are described within a pair interaction approximation, based on effective cation-cation pair energies E_i^{FeV}, E_i^{FeFe} and E_i^{VV} with

$i = 1$, 2, and 3 denoting first, second and third-neighbor cationic pairs, respectively. Within this approximation, the distribution of cations is driven by effective mixing parameters $W_i = 2E_i^{FeV} - E_i^{FeFe} - E_i^{VV}$ which account for the energy gain (or expense) to form two Fe-V pairs in place of one Fe-Fe and one V-V pair (at a given i distance). $W < 0$ and $W > 0$ are indicative for mixing (preference for Fe-V pairs) and phase separation (preference for Fe-Fe and V-V pairs), respectively.

The MC simulations have been performed using W_i values deduced from DFT calculations on model configurations: the ordered ones at x = 0.125, 0.25, 0.375 and 0.5 (SI, Section S2.2, Fig. S3), and configurations at x = 0.25 with the Fe-Fe pair in first-, second- or third-neighbor positions. We find W_1 = -0.5 ± 0.01 eV, W_2 = -0.06 ± 0.01 eV and W_3 more than one order of magnitude smaller than W_2. The MC simulations have thus been performed with $W_3/W_1 = 0.00$, $W_2/W_1 = 0.12$ and $k_BT/|W_1| = 0.10$, the latter value being consistent with the experimental annealing temperature $T \approx 600$ K. We have additionally checked that the results are robust with respect to variations (±0.02) of both $k_BT/|W_1|$ and W_2/W_1 (SI, Section S3, Fig. S5).

Standard importance sampling MC simulations were carried out for each Fe concentration on a periodic 10 × 10 cationic honeycomb lattice (containing 200 cationic sites). A Metropolis algorithm drives trial exchanges between Fe and V atoms, with 50 000 000 Monte Carlo steps per site. Neglecting the first 500 000 steps in each run, average structural characteristics of the cation distribution were evaluated and snapshots of the final configurations were kept. We have additionally checked that our results are robust with respect to the choice of the MC periodic unit cell (SI, Section S3, Fig. S5).

3 Results

3.1 General features

To demonstrate V/Fe intermixing in the honeycomb lattice, samples were prepared by reactive deposition of pure V and Fe/V mixtures onto the Pt(111) surface. Figure 2 displays LEED measurements of pure V and mixed V/Fe oxides, the latter with an approximate iron content $x \approx 0.25$. In both cases, a sharp (2×2) pattern is revealed next to the hexagonal (1×1) Pt spots. As no oxygen superstructure is formed on Pt(111) at the experimental conditions,[50] the (2×2) reflexes clearly indicate the formation of commensurate oxide ad-layers. The lattice parameter of 5.54 × 5.54 Å^2 is hereby identical for the two oxide phases. In associated STM images, wide monolayer islands of 10-20 nm diameter, 1.5 Å height and roundish shapes are detected for the binary and mixed oxide layers (Figs. 2 a, b). Both films crystallize in a perfect honeycomb lattice, with the cationic positions being detected at positive sample bias (Figs. 2 d, f). In the case of the binary oxide, it is readily assigned to a V_2O_3 monolayer, similar to that observed on Pd(111).[51]

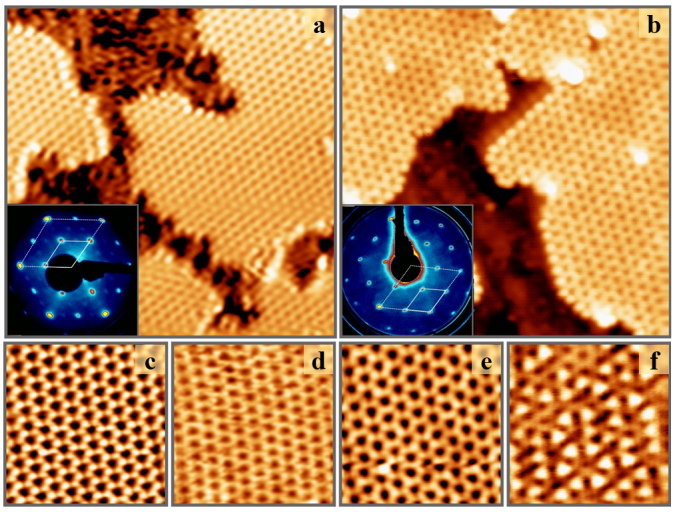

Figure 2: STM overview images of (a) pure V_2O_3 and (b) mixed $(V_{0.75}Fe_{0.25})_2O_3$ honeycomb films on Pt(111) (U_B = 0.5 V, I = 0.1 nA, 15 × 15 nm^2). The insets show corresponding LEED patterns (E_{kin} = 100 eV) with the oxide and substrate cells marked by solid and dashed rhombs, respectively. High resolution images of pure, (c) U_B = 0.1 V, (d) U_B = 1.5 V, and mixed (e) U_B = 0.1 V, (f) U_B = 1.5 V oxide films (5 × 5 nm^2).

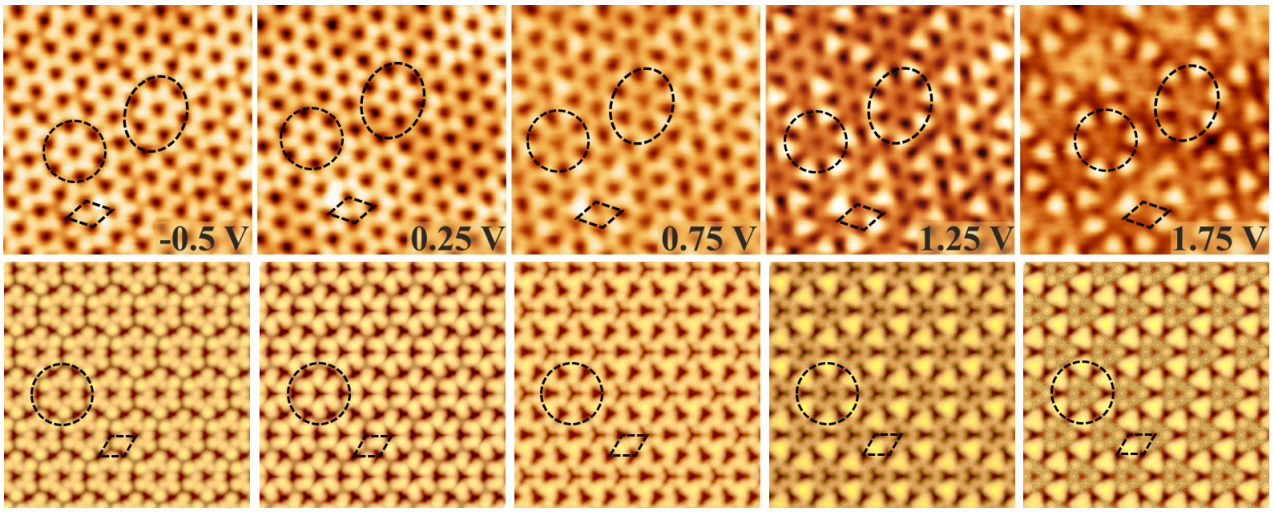

Figure 3: Topographic (top) and simulated (bottom) STM images ($I = 0.1$ nA; 5×5 nm^2) of mixed oxide honeycomb films with 25 % Fe content, obtained at different bias values. Large rings formed by Fe atoms in third-neighbor positions are indicated in each panel, together with the (2×2)-Pt(111) unit cell.

3.2 Cation differentiation

While the STM contrast of the pure V_2O_3 honeycomb film shows virtually no bias dependence, the different chemical identity of cations in the mixed oxide film becomes visible at higher bias, Fig. 3 (top panels). Indeed, above 1.0 V, the V species show diminishing contrast, while the Fe ions and the Fe-bound oxygen appear brighter and develop a characteristic triangular shape in the topographic images. The two triangular orientations in the measurements reflect Fe species bound to either hcp or fcc sites of the Pt(111) support. On the basis of such images, the stoichiometry of the mixed oxide films is accessible to the experiment. Conversely, information on the anionic lattice is obtained at negative bias, when tunneling out of the O 2p orbitals dominates the STM contrast (SI, Section S1, Fig. S2). As expected, a Kagome lattice of the O ions is resolved, whereby the contrast is dominated by those O-triples that surround the Fe-species.

Simulated STM images, Fig. 3 (bottom panels), of an ordered $V_6Fe_2O_{12}$/(4x4)-Pt(111) configuration with the two iron atoms in third-neighbor positions, account very well for the observed contrast behavior: (i) at negative bias (-0.5 V) mostly O ions contribute to the STM contrast, (ii) at small positive bias (+0.25 V, +0.75) both types of cations are visible, and (iii) as the bias increases (+1.25 V, +1.75 V) the Fe cations and neighboring O atoms produce the characteristic triangular signature, whereas the contrast due to V cations diminishes. The DFT simulations provide insights into the competition between structural and electronic effects responsible for such contrast characteristics.

From a structural point of view, Fig. 4 a, b, all cations are 3-fold coordinated and sit in the hollow (either hcp or fcc) sites of the Pt(111) surface, whereas anions are 2-fold coordinated and are located on top of the surface Pt atoms. Fe cations are positioned 0.10 Å closer to the substrate than V ones, while the anions are virtually co-planar (± 0.005 Å) and relax substantially outward with respect to cations. This gives rise to a noticeable film rumpling of about 0.75 Å which accommodates a large part of the lattice mismatch. The remaining in-plane compressive strain is accommodated by small rotations of the MO_3 units.

The electronic structure of the mixed oxide monolayer, Fig. 4 c and Tab. S2 in SI (Section S2.2), is characterized by an absence of V nonbonding d states below the Fermi level and a vanishing V magnetic moment which concomitantly provide a clear signature of vanadium 5+

formal oxidation state. Such strong increase of the oxidation state compared to that in the free-standing V_2O_3 ML (in which V is undoubtedly 3+), is due to a large electron transfer from V to the strongly electronegative Pt substrate. In contrast, the local density of states (LDOS) of Fe atoms, as well as their charges and magnetic moments preserve a character akin to Fe^{3+} in pure Fe_2O_3 systems (SI, Section S2.1, Tab. S1).

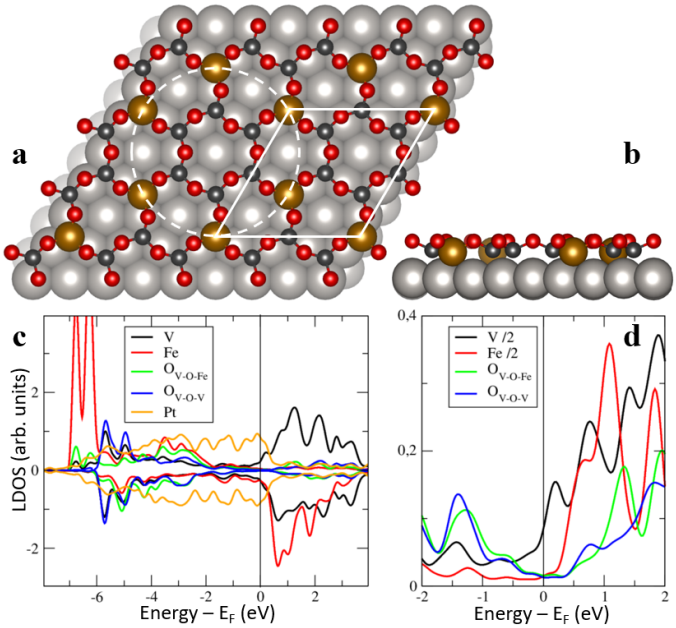

Figure 4: Top (a) and side (b) views of the atomic structure of 1ML $V_6Fe_2O_{12}$/(4×4)-Pt(111) configuration. V, Fe, O, and Pt atoms are plotted with black, golden, red, and gray balls, respectively. The (4×4) unit cell and a large ring formed by Fe atoms in 3rd-neighbor positions are indicated. (c) Spin-resolved atom-projected densities of states. Spin-up and -down LDOS are plotted with positive and negative values, respectively. (d) Zoom of the spin-averaged cation d_{z^2} and anion p_z LDOS in the vicinity of the Fermi level.

The STM contrast as a function of bias is conventionally linked to features in the O p_z and cation d_{z^2} LDOS which dominate the interaction with the STM tip. Fig. 4 d reveals a comparatively important anion LDOS below the Fermi level which is responsible for the Kagome lattice seen at negative bias. Conversely, the LDOS above the Fermi level is dominated by cation contributions. In particular, the Fe d_{z^2} LDOS displays a maximum at about 1.1 eV, which is directly responsible for the progressive increase of the STM contrast of Fe cations. However, the positive-bias contrast is also influenced by anions due to their larger elevation with respect to the substrate and the less localized atomic character of p compared to d orbitals. In particular, the oxygen atoms which bridge a V and a Fe cation (O_{V-O-Fe}) are characterized by a LDOS maximum at about 1.2 eV, which is responsible for the triangular STM signature of Fe cations. Interestingly, similar maxima are also present in the d_{z^2} LDOS of V cations and of oxygen atoms bridging two V cations (O_{V-O-V}), but at somewhat higher energies. Thus, the differentiation of the V and Fe cations in STM is mainly due to the lower energy of the Fe d_{z^2} orbital and of the corresponding feature in the O_{V-O-Fe} LDOS, driven by a stronger localization of the d orbitals in Fe than in V.

In a wider perspective, by means of DFT calculations, we have checked that these structural and electronic characteristics are fairly robust when the Fe concentration is varied between $0 < x \leq 0.5$, (SI, Section S2.2, Tab. S2). Most importantly, the cation charges and magnetic moments are quasi-constant in the series, indicating that the 5+ and 3+ formal oxidation states of the V and Fe cations persist regardless the film composition. This conclusion is further confirmed by the quasi-linear variation of the Pt charge along the series due to the linearly decreasing proportion of V cations in Fe-rich films.

3.3 Fe distribution as a function of concentration

Beyond the results at $x = 0.25$ presented above, in this section we analyze the distribution of cations in the mixed $(V_{1-x}Fe_x)_2O_3$ MLs at various Fe concentrations, as obtained by STM imaging and Monte Carlo simulations. We focus on films with compositions $x < 0.5$, because the experiments show that, at a Fe content of about 48%, the cationic mixing comes to an end, and phase separation takes place in which the mixed honeycomb ML coexists with other

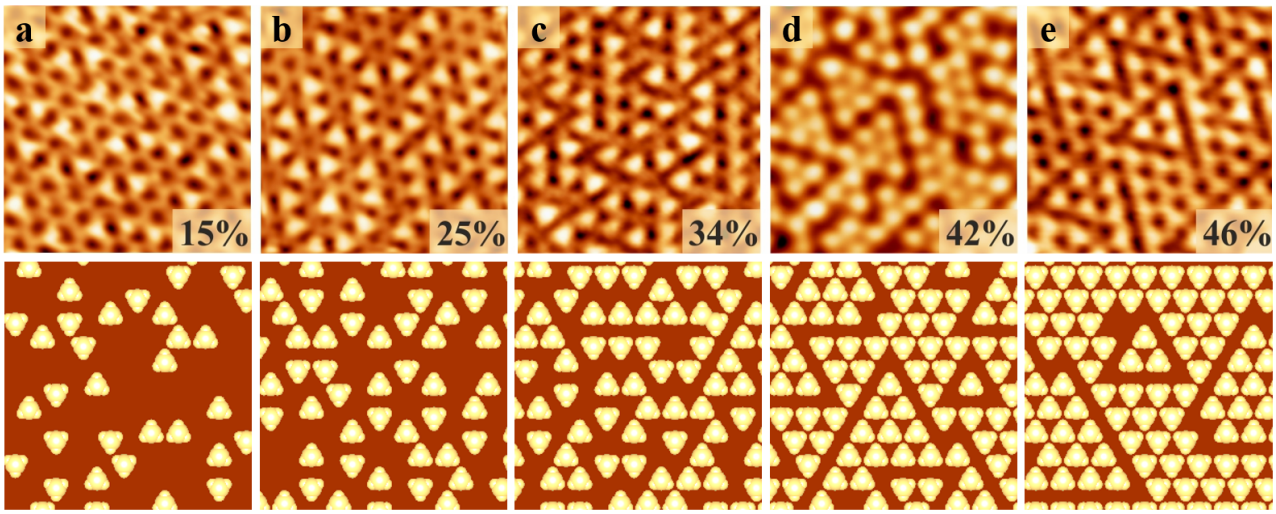

Figure 5: Topographic STM images (U_B = 1.5 V; 5 ×5 nm^2) (a) and snapshots of Monte Carlo simulations (b) of mixed honeycomb oxides at increasing Fe concentrations x.

oxide phases (SI, Section S1, Fig. S1). We will come back to the reasons for such upper concentration limit in the Discussion Section.

Figure 5 (top panels) shows STM topographic images of $(V_{1-x}Fe_x)_2O_3$ MLs synthesized on Pt(111) at $x \approx 0.15$, 0.25, 0.34, 0.42 and 0.46 and MC snapshots obtained at the same Fe concentrations (bottom panels). It evidences an excellent agreement between experiment and theory. Moreover, we substantiate the qualitative information from STM images and MC snapshots by quantitative results on the cation distribution in the lattice, displayed in Fig. 6, and link them to the energetics of the system: W_1 = -0.50 eV, W_2 = -0.06 eV and $W_3 \approx 0.00$ eV. Note the very satisfactory matching between measured and calculated characteristics in Fig. 6 b.

The most important finding of both experiment and calculations is the quasi absence of first-neighbor Fe-Fe pairs whatever the film composition. This observation is confirmed by the nearly constant value of $N_1 \approx 3$ (Fig. 6 a), which tells that the three cationic sites adjacent to each Fe cation are systematically occupied by V ions. Such preference is consistent with the large negative value of W_1 which strongly favors mixed (V-Fe) first-neighbor pairs. In the following, we will thus focus on the distribution of second- and third-neighbor cation-cation pairs.

At the lowest Fe content, Figure 5 a, isolated (i) Fe ions are randomly distributed in the V_2O_3 honeycomb lattice, with, in average, 6 second- ($N_2 \approx 6$) and 3 third- ($N_3 \approx 3$) V neighbors, Fig. 6 a. This is consistent with the preference for mixed Fe-V second-neighbor pairs ($W_2 < 0$).

As the Fe concentration increases, a growing fraction of Fe atoms has at least one Fe third-neighbor in para (p) position ($N_3 < 3$, Figs. 6 a and b), and the number of isolated Fe atoms diminishes progressively until it vanishes at $x \approx 0.2$. As x gets closer to 0.25, third-neighbor Fe-Fe pairs progressively give rise to the formation of Fe rings with ≈ 12.5 Å diameter surrounding a pure V_6O_6 honeycomb ring (Fig. 5 b). The underlying fully ordered structure, with each Fe atom having only V cations as first and second neighbors and only Fe ions as third neighbors ($N_1 = 3$, $N_2 = 6$ and N_3=0) corresponds to the configuration which has been analyzed in details in the preceding Section, Fig. 4. Since $W_3 \approx 0$, this structure enables the most dense packing of Fe cations in the V_2O_3 honeycomb lattice with no unfavorable (ortho or meta) Fe-Fe pairs. It is expected to form at lower temperatures, as shown in SI, Section S3.

A further increase of x leads to a larger fraction of second-neighbor Fe-Fe pairs assembled in chains of rather short length, Fig. 5 c. The number of Fe atoms (c) in the chains reaches a maximum around $x = 0.27$, Fig. 6 b.

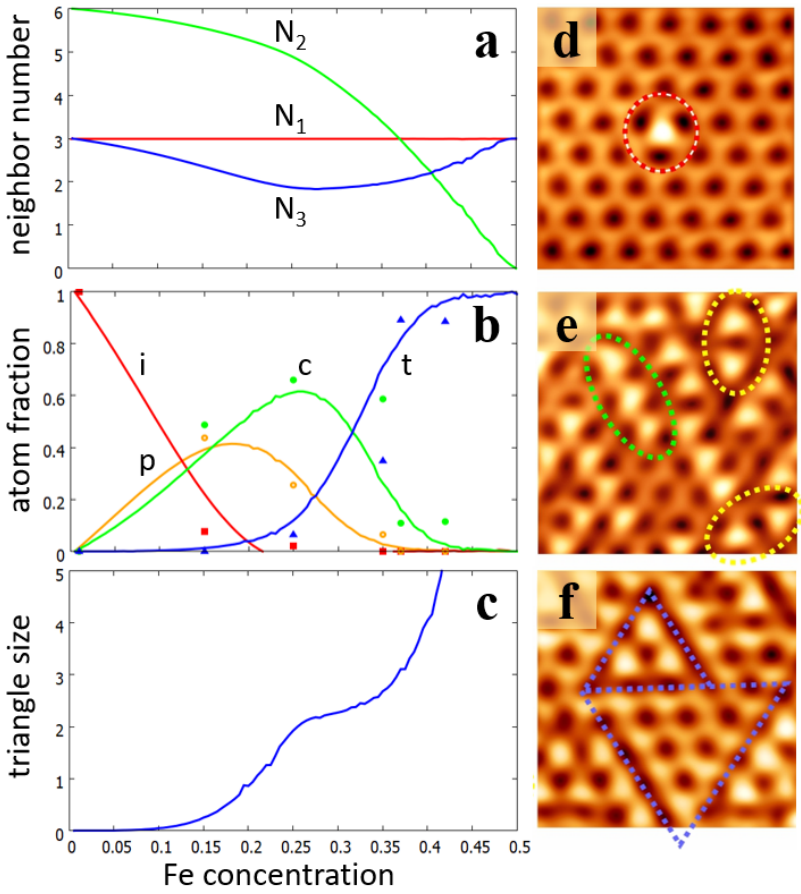

Figure 6: Main characteristics of the cation distribution in the mixed oxide films as a function of Fe concentrations, from MC simulations: (a) average number of first-, second- and third-neighbor V-Fe pairs (N_1, N_2 and N_3); (b) fraction of Fe atoms in isolated (i), para Fe-Fe pairs (p), chain (c), and triangular (t) configurations. The symbols reflect experimental data, averaged over several STM images; (c) average lateral size of the Fe triangles (number of Fe atoms along triangle edge). STM topographic images ($U_B = 1.5$ V, $I = 0.1$ nA, 3.6×3.6 nm^2) show (d): an isolated Fe atom, (e): third-neighbor Fe-Fe pairs (yellow) and short Fe chains (green), and (f): Fe triangular structures separated by boundaries made of Fe ions in para positions of the honeycomb rings (blue).

A larger increase of the number of Fe atoms results in meta Fe-Fe pairs, forming triangular domains which consist in a lattice of alternating Fe and V ions ($N_2 \approx 0$, $N_3 \approx 3$), and are separated from one another by zig-zag boundaries with Fe ions in para-positions of the honeycomb rings (Fig. 5 d). The triangle sizes remain relatively small (less than $\approx 3-4$ Fe atoms along each edge) up to the maximum concentration experimentally attainable. The preference for small triangles over larger ones is substantiated by the existence of a plateau at a mean triangle edge size of ≈ 2.5 atoms ($0.25 < x < 0.35$), Fig. 6 c. It can be linked to the fact that the number of unfavorable second-neighbor Fe-Fe pairs per Fe atom increases with the triangle size (1.0, 1.5, 1.8 and 2.0 for sizes 2, 3, 4 and 5, respectively).

At higher concentrations, Fig. 5 e, neighboring triangles overlap and it is no longer possible to unambiguously determine their size. Finally, at $x = 0.5$, MC simulations on the cationic honeycomb lattice find a periodically ordered (2×2) structure ($N_2 = 0$, $N_3 = 3$), corresponding to the total suppression of boundaries between the triangles.

4 Discussion

4.1 Stability of the mixed phase

The overall stability of the supported mixed monolayers can be assessed from their formation energies E_{form} (per oxide f.u.). Consistently with the presence of FeO_x particles for $x \gtrsim 0.5$ (SI, Section S1, Fig. S1), the E_{form} have been calculated with respect to the two corresponding bulk V_2O_3 and Fe_2O_3 parents, which may also serve as references for oxide particles or thicker oxide films:

$$4E_{form} = E(V_{8-n}Fe_nO_{12}/Pt) - E(Pt) - \frac{(8-n)}{2}E_{bulk}(V_2O_3) - \frac{n}{2}E_{bulk}(Fe_2O_3) \quad (1)$$

with $E(V_{8-n}Fe_nO_{12}/Pt)$ and $E(Pt)$ being the total energy of the supported $V_{8-n}Fe_nO_{12}$ monolayer and of the bare Pt slab, respectively, whereas $E_{bulk}(V_2O_3)$ and $E_{bulk}(Fe_2O_3)$ represent the total energies (per f.u.) of V_2O_3 and Fe_2O_3 bulk oxides, respectively. Factor four accounts for the number of oxide formula units in the (4×4)-Pt(111) surface unit cell. With this definition, formation energies are negative if the supported mixed layer is favored with respect to the corresponding bulks.

We find that the formation energies of the Pt-supported mixed monolayers are equal to -0.14, -0.18, -0.14, -0.05, +0.27, +0.52, and +0.93 eV/f.u. for Fe concentrations $x = 0.125$, 0.25, 0.375, 0.5, 0.625, 0.75, and 0.875, respectively. They are thus negative for $0 < x \leq 0.5$, indicating the energetic preference for mixed supported films, which is consistent with the experimental observations. For Fe contents beyond 0.5, the formation energy becomes positive, in agreement with the absence of mixed Fe-rich monolayers in the experiment.

The destabilization of mixed layers upon an increase of the Fe content is due to the weak interaction between the Pt substrate and the Fe_2O_3 monolayer (1ML Fe_2O_3/Pt is less stable than bulk Fe_2O_3 by 1.2 eV/Fe_2O_3). It contrasts with the strong stabilization of 1ML V_2O_3 by the Pt substrate, consistent with its experimental observation (1ML V_2O_3/Pt is 0.1 eV/V_2O_3 more stable than V_2O_3 bulk).[52] Such a difference finds its roots in the very different electron transfers between Fe_2O_3 and V_2O_3 and the Pt substrate, which are driven by the relative position of the Fermi levels of the corresponding freestanding layers with respect to Pt(111).[33] The Fe_2O_3 layer is insulating and the Pt Fermi level is located in its gap, a configuration not prone to electron exchange. In contrast, the Fermi level of the freestanding metallic V_2O_3 layer sits about 1.5 eV above that of Pt, which rationalizes the strong electron transfer towards the support, the formation of V^{5+} cations and the sizable stabilization of the V_2O_3 monolayer.

4.2 Origin of cation-cation interaction

We have seen that the tendency for V-Fe mixing over phase separation in Pt-supported monolayers is driven by the strong energetic preference for mixed V-Fe first-neighbor pairs over

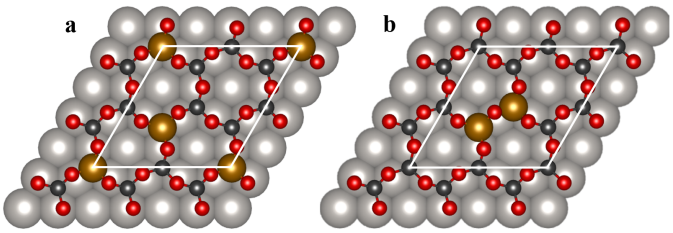

Figure 7: Top views of the atomic structure of 1ML $V_6Fe_2O_{12}$/(4x4)-Pt(111) configurations in which two Fe cations occupy either (a) third- or (b) first-neighbor positions in the V_2O_3 honeycomb monolayer. V, Fe, O, and Pt atoms are represented with black, golden, red, and gray balls, respectively.

V-V and Fe-Fe ones (W_1 = -0.5 eV). Its origin may be assessed by comparing configurations in which two Fe cations occupy either first- or third-neighbor positions, Figs. 7 a and b. In these MLs, due to the nearly vanishing value of W_3, the energy cost δE of moving the two Fe cations next to each other is equal to $-W_1$, a positive quantity that reflects an effective Fe-Fe repulsion. The DFT results reveal that, although the transformation of one configuration into the other preserves the number of atoms of each type, the film structure, and the number of cation-oxygen and cation-Pt bonds, the total energies of the two configurations do indeed differ by $\delta E = 0.5$ eV.

As shown in Table S3 (SI, Section S2.3), the two configurations have very similar electronic characteristics. However, their atomic structures differ (SI, Fig. S4), because approaching two Fe cations leads to a reduction of two Fe-O distances and an expansion of two V-O bonds. Since the energetic cost of these distortions cannot be easily quantified, we have performed an additional DFT simulation of the same two configurations with the two Fe cations placed in a rigid V_2O_3/Pt lattice. This constraint allows the first-neighbor environments (cation-anion and cation-substrate distances) of all cations to be exactly the same in the two configurations. We find that the electronic characteristics (charges of all cations, anions and Pt) of the two configurations do not differ by more than 0.01 e, and remain very close (within 0.03 e) to those in the corresponding fully relaxed structures. In contrast, the δE value between the two constrained configurations is equal to 0.35 eV, which accounts for as much as 70% of the fully relaxed result (δE = 0.5 eV). This clearly demonstrates that strain effects and short-range covalent contributions do not play a dominant role in the repulsive Fe-Fe interaction.

Therefore, the principal effect consists of the existence of Fe-Fe and V-V first-neighbor cation pairs (when the two Fe atoms are close to each other) in place of two Fe-V ones (when the two Fe atoms are distant). While first-neighbor cation-cation distances ($\approx$ 3.2 Å) do not enable chemical bond formation, the large cationic charges imply the existence of electrostatic repulsion. In this respect, replacing two Fe^{3+}-V^{5+} pairs by one Fe^{3+}-Fe^{3+} and one V^{5+}-V^{5+} is indeed unfavorable from an electrostatic point of view. Similar conclusion may be drawn from an explicit Ewald summation using Bader charges issued from the DFT calculations for O, Fe, V atoms and the Pt substrate. It confirms that the strong preference for mixed first-neighbor V-Fe pairs is mediated by electrostatic interactions. It is important to stress that this effect relies on the difference in oxidation states of V and Fe and is thus induced by the strong electron transfer from V to the Pt substrate.

4.3 Two-dimensional oxide nanoalloy

In order to establish a link between alloy formation and reduced dimensionality in $(V,Fe)_2O_3$ oxides, we have calculated the same energy cost δE of moving two Fe cations from third- to first-neighbor positions in: (i) a fully relaxed freestanding $V_6Fe_2O_{12}$ monolayer and (ii) the same monolayer embedded in bulk V_2O_3.

Similarly to the Pt-supported case, we find a large positive δE = 0.7 eV in the freestanding monolayer, while $\delta E \approx 0$ is nearly vanishing in the bulk oxide. The computational results thus demonstrate a significant difference in mixing behavior as a function of dimensionality. The strong bias for V-Fe mixing is limited to the honeycomb monolayers, whether supported or not, and does not exist in bulk-like oxide, con-

sistent with the absence of $VFeO_3$ bulk oxides in nature.

The effect can be traced back to the different electronic characteristics of the cations in these two cases. On the one hand, we find that in monolayers some cations change their oxidation state. In the freestanding monolayer, the Fe Bader charges and magnetic moments are consistent with a reduced formal oxidation state, Fe^{2+}, whereas the oxidation state of some V cations tends to increase to V^{4+}. The internal electron transfer from V to Fe is driven by a substantial offset between their electronic states,[32] unlike in the supported case where it occurs from V to Pt.

On the other hand, in contrast, we find that in the bulk, all cations preserve their +3 oxidation states typical for corundum bulk V_2O_3 and Fe_2O_3. The absence of electron exchange between the two cations is due to a larger gap in bulk Fe_2O_3, which pushes the empty Fe states to higher energies.[20]

The results therefore demonstrate the truly nanoscale character of the $(V,Fe)_2O_3$ alloy monolayers. Not only is the observed tendency for V-Fe mixing limited to the two-dimensional (2D) layers, but it is also tightly linked to a change of cation oxidation states. These 2D nanoalloys thus display unique electronic characteristics compared to what would be a mere average of their bulk parents properties.

5 Conclusion

We report successful preparation of a mixed $(V_{1-x}Fe_x)_2O_3$ honeycomb film on the Pt(111) substrate, stable in a large span of stoichiometries ($0 < x \lesssim 0.5$) and at realistic temperatures. A thorough atomic scale STM characterization that enabled a clear differentiation between the V and Fe cations, due to a specific triangular contrast pattern of the latter, allowed the direct determination of the cation distribution as a function of film composition. DFT calculations rationalized the observed STM contrast as a function of applied bias and provided cation-cation mixing parameters which have been further used in MC simulations of the cation distributions. Both, the DFT and MC results were found to be in very good agreement with measurements.

Our results demonstrate the mixed character of the $(V,Fe)_2O_3$/Pt film. We assign it to an energetic preference for the formation of V-Fe pairs, particularly strong for cations in first-neighbor positions, but still non-negligible for the second-neighbors. The DFT calculations prove that the thermodynamic stability of the alloy is principally driven by the strong interaction between the V_2O_3 film and the Pt(111) substrate, that results in different charge states for the V and Fe cations and produces a strong bias toward cationic mixing.

Dedicated DFT analysis has enabled a comparison between mixing characteristics in nanoscale and bulk-like $(V,Fe)_2O_3$ oxides. It shows that not only is the observed tendency for V-Fe mixing limited to 2D monolayers, but that it is also tightly linked to a change of cation oxidation states, which makes their electronic characteristics different from those of the corresponding pure bulk materials. This convincingly confers a nanoalloy character to the fabricated $(V,Fe)_2O_3$/Pt honeycomb films and shows that, well beyond massive materials, the flexibility of their composition, cation distribution and charge state provide levers for tailoring the properties of oxide nano-materials and thus may enhance their applicative potential.

6 Conflict of Interest

The authors declare no conflicts of interest

7 Acknowledgment

There is no financial support to disclose

8 Supplementary Information Available

The Supporting Information contains:

- Additional STM images of (i) phase mixtures at high Fe content and (ii) the

Kagomé lattice of the oxygen anions at $x \approx 0.2$.

- Additional DFT results including (i) bulk and freestanding $VFeO_3$ properties; (ii) supported film characteristics as a function of Fe concentration; (iii) configurations for the determination of Fe-Fe interactions.
- Additional MC results at various unit cell sizes, temperatures $k_BT/|W_1|$, and W_2/W_1 parameters.

References

(1) Lorenz, M.; Rao, M. R.; Venkatesan, T.; Fortunato, E.; Barquinha, P.; Branquinho, R.; Salgueiro, D.; Martins, R.; Carlos, E.; Liu, A. et al. The 2016 oxide electronic materials and oxide interfaces roadmap. *J. Phys. D: Appl. Phys.* **2016**, *49*, 433001.

(2) Coll, M.; Fontcuberta, J.; Althammer, M.; Bibes, M.; Boschker, H.; Calleja, A.; Cheng, G.; Cuoco, M.; Dittmann, R.; Dkhil, B. et al. Towards oxide electronics: a roadmap. *Appl. Surf. Sci.* **2019**, *482*, 1–93.

(3) Netzer, F. P.; Noguera, C. *Oxide thin films and nanostructures*; Oxford University Press, 2021.

(4) Noguera, C.; Fritz, B. In *Encyclopedia of Geochemistry: A Comprehensive Reference Source on the Chemistry of the Earth*; White, W. M., Ed.; Springer International Publishing: Cham, 2017; pp S:1–8.

(5) Smallman, R. E.; Bishop, R. J. *Modern physical metallurgy and materials engineering*; Butterworth-Heinemann, 1999.

(6) Ducastelle, F.; Legrand, B.; Tréglia, G. Surface segregation in transition metal alloys: from electronic structure to phase portraits. *Prog. Theor. Phys. Suppl.* **1990**, *101*, 159–180.

(7) Ohtomo, A.; Tsukazaki, A. Pulsed laser deposition of thin films and superlattices based on ZnO. *Semicond. Sci. Technol.* **2005**, *20*, S1.

(8) Vasala, S.; Karppinen, M. $A_2B'B''O_6$ perovskites: a review. *Prog. Solid State Chem.* **2015**, *43*, 1–36.

(9) Zhu, Y.; Tahini, H. A.; Hu, Z.; Dai, J.; Chen, Y.; Sun, H.; Zhou, W.; Liu, M.; Smith, S. C.; Wang, H. et al. Unusual synergistic effect in layered Ruddlesden- Popper oxide enables ultrafast hydrogen evolution. *Nature Comm.* **2019**, *10*, 1–9.

(10) Bibes, M.; Barthelemy, A. Oxide spintronics. *IEEE Trans. Electron Devices* **2007**, *54*, 1003–1023.

(11) Šutka, A.; Gross, K. A. Spinel ferrite oxide semiconductor gas sensors. *Sens. Actuators, B* **2016**, *222*, 95–105.

(12) Védrine, J. C. Heterogeneous catalysis on metal oxides. *Catalysts* **2017**, *7*, 341.

(13) McFarland, E. W.; Metiu, H. Catalysis by doped oxides. *Chem. Rev.* **2013**, *113*, 4391–4427.

(14) Bates, M. K.; Jia, Q.; Doan, H.; Liang, W.; Mukerjee, S. Charge-transfer effects in Ni–Fe and Ni–Fe–Co mixed-metal oxides for the alkaline oxygen evolution reaction. *ACS Catalysis* **2016**, *6*, 155–161.

(15) Rodriguez, J.; Jirsak, T.; Pérez, M.; González, L.; Maiti, A. Studies on the behavior of mixed-metal oxides: Adsorption of CO and NO on MgO (100), $Ni_xMg_{1-x}O$ (100), and $Cr_xMg_{1-x}O$ (100). *J. Chem. Phys.* **2001**, *114*, 4186–4195.

(16) Nilius, N.; Freund, H.-J. Activating nonreducible oxides via doping. *Acc. Chem. Res.* **2015**, *48*, 1532–1539.

(17) Davies, P.; Navrotsky, A. Quantitative correlations of deviations from ideality in binary and pseudobinary solid solutions. *J. Solid State Chem.* **1983**, *46*, 1–22.

(18) Allan, N.; Barrera, G.; Fracchia, R.; Lavrentiev, M. Y.; Taylor, M.; Todorov, I.; Purton, J. Free energy of solid solutions and phase diagrams via quasiharmonic lattice dynamics. *Phys. Rev. B* **2001**, *63*, 094203.

(19) Benny, S.; Grau-Crespo, R.; de Leeuw, N. H. A theoretical investigation of α-Fe_2O_3–Cr_2O_3 solid solutions. *Phys. Chem. Chem. Phys.* **2009**, *11*, 808–815.

(20) Le, H.-L. T.; Goniakowski, J.; Noguera, C. Properties of mixed transition metal oxides: MM'O_3 in corundum-type structures (M, M' = Al, Ti, V, Cr, and Fe). *Phys. Rev. Mat.* **2018**, *2*, 085001.

(21) Ferrando, R.; Jellinek, J.; Johnston, R. L. Nanoalloys: from theory to applications of alloy clusters and nanoparticles. *Chem. Rev.* **2008**, *108*, 845–910.

(22) Gionco, C.; Paganini, M. C.; Agnoli, S.; Reeder, A. E.; Giamello, E. Structural and spectroscopic characterization of CeO_2–TiO_2 mixed oxides. *J. Mater. Chem. A* **2013**, *1*, 10918–10926.

(23) Stankic, S.; Suman, S.; Haque, F.; Vidic, J. Pure and multi-metal oxide nanoparticles: synthesis, antibacterial and cytotoxic properties. *J. Nanobiotechnol.* **2016**, *14*, 73.

(24) Cuko, A.; Calatayud, M.; Bromley, S. T. Stability of mixed-oxide titanosilicates: dependency on size and composition from nanocluster to bulk. *Nanoscale* **2018**, *10*, 832–842.

(25) Stacchiola, D.; Kaya, S.; Weissenrieder, J.; Kuhlenbeck, H.; Shaikhutdinov, S.; Freund, H.-J.; Sierka, M.; Todorova, T. K.; Sauer, J. Synthesis and structure of ultrathin aluminosilicate films. *Angew. Chem., Int. Ed.* **2006**, *45*, 7636–7639.

(26) Jerratsch, J. F.; Nilius, N.; Freund, H.-J.; Martinez, U.; Giordano, L.; Pacchioni, G. Lithium incorporation into a silica thin film: Scanning tunneling microscopy and density functional theory. *Phys. Rev. B* **2009**, *80*, 245423.

(27) Maria Zollner, E.; Schuster, F.; Meinel, K.; Stötzner, P.; Schenk, S.; Allner, B.; Förster, S.; Widdra, W. Two-dimensional wetting layer structures of reduced ternary oxides on Ru (0001) and Pt (111). *Phys. Stat. Solidi (b)* **2020**, *257*, 1900655.

(28) Wu, C.; Castell, M. R.; Goniakowski, J.; Noguera, C. Stoichiometry engineering of ternary oxide ultrathin films: $Ba_xTi_2O_3$ on Au(111). *Phys. Rev. B* **2015**, *91*, 155424.

(29) Lockhorn, M.; Kasten, P. E.; Tosoni, S.; Pacchioni, G.; Nilius, N. Growth and characterization of Ca—Mo mixed oxide films on Mo (001). *J. Chem. Phys.* **2019**, *151*, 234708.

(30) Pomp, S.; Kuhness, D.; Barcaro, G.; Sementa, L.; Mankad, V.; Fortunelli, A.; Sterrer, M.; Netzer, F. P.; Surnev, S. Two-dimensional iron tungstate: A ternary oxide layer with honeycomb geometry. *J. Phys. Chem. C* **2016**, *120*, 7629–7638.

(31) Rodríguez-Fernández, J.; Sun, Z.; Zhang, L.; Tan, T.; Curto, A.; Fester, J.; Vojvodic, A.; Lauritsen, J. V. Structural and electronic properties of Fe dopants in cobalt oxide nanoislands on Au (111). *J. Chem. Phys.* **2019**, *150*, 041731.

(32) Goniakowski, J.; Noguera, C. Intrinsic properties of pure and mixed monolayer oxides in the honeycomb structure: M_2O_3 and MM'O_3 (M, M' = Ti, V, Cr, Fe). *J. Phys. Chem. C* **2019**, *123*, 7898–7910.

(33) Goniakowski, J.; Noguera, C. Properties of Metal-Supported Oxide Honeycomb Monolayers: M_2O_3 and MM' O_3 on Me (111)(M, M'= Ti, V, Cr, Fe; Me= Ag, Au, Pt). *J. Phys. Chem. C* **2020**, *124*, 8186–8197.

(34) Kresse, G.; Furthmuller, J. Efficient iterative schemes for ab initio total energy calculations using a plane-wave basis set. *Phys. Rev. B* **1996**, *54*, 11169–11186.

(35) Kresse, G.; Hafner, J. Ab initio molecular dynamics for liquid metals. *Phys. Rev. B* **1993**, *47*, 558–561.

(36) Blöchl, P. E. Projector augmented-wave method. *Phys. Rev. B* **1994**, *50*, 17953–17979.

(37) Kresse, G.; Joubert, D. From ultrasoft pseudopotentials to the projector augmented-wave method. *Phys. Rev. B* **1999**, *59*, 1758–1775.

(38) Dion, M.; Rydberg, H.; Schroder, E.; Langreth, D. C.; Lundqvist, B. I. Van der Waals density functional for general geometries. *Phys. Rev. Lett.* **2004**, *92*, 246401.

(39) Klimes, J.; Bowler, D. R.; Michaelides, A. Chemical accuracy for the van der Waals density functional. *J. Phys.: Condens. Matter* **2010**, *22*, 022201.

(40) Klimes, J.; Bowler, D. R.; Michaelides, A. Van der Waals density functionals applied to solids. *Phys. Rev. B* **2011**, *83*, 195131.

(41) Anisimov, V. I.; Aryasetiawan, F.; Liechtenstein, A. I. First-principles calculations of the electronic structure and spectra of strongly correlated systems: the LDA+U method. *J. Phys.: Condens. Matter* **1997**, *9*, 767–808.

(42) Dudarev, S. L.; Botton, G. A.; Savrasov, S. Y.; Humphreys, C. J.; Sutton, A. P. Electron-energy-loss spectra and the structural stability of nickel oxide: An LSDA+U study. *Phys. Rev. B* **1998**, *57*, 1505–1509.

(43) Le, H.-L.; Goniakowski, J.; Noguera, C. (0001) Interfaces between M_2O_3 corundum oxides (M = Al, Ti, V, Cr, Fe). *Surf. Sci.* **2019**, *679*, 17–23.

(44) Goniakowski, J.; Noguera, C. Properties of M_2O_3/Au(111) honeycomb monolayers (M = Sc, Ti, V, Cr, Mn, Fe, Co, Ni). *J. Phys. Chem. C* **2019**, *123*, 9272–9281.

(45) Bader, R. F. W. A quantum theory of molecular structure and its applications. *Chem. Rev.* **1991**, *91*, 893–928.

(46) Henkelman, G.; Arnaldsson, A.; Jonsson, H. A fast and robust algorithm for Bader decomposition of charge density. *Comput. Mater. Sci.* **2006**, *36*, 354–360.

(47) Tersoff, J.; Hamann, D. R. Theory of the scanning tunneling microscope. *Phys. Rev. B* **1985**, *31*, 805.

(48) Momma, K.; Izumi, F. VESTA 3 for three-dimensional visualization of crystal, volumetric and morphology data. *J. Appl. Crystallogr.* **2011**, *41*, 1272–1276.

(49) Monkhorst, H.; Pack, J. Special points for Brillouin-zone integrations. *Phys. Rev. B* **1976**, *13*, 5188–5192.

(50) Szabo, A.; Kiskinova, M.; Yates Jr, J. Carbon monoxide–oxygen interaction on the Pt (111) surface: An electron stimulated desorption ion angular distribution (ESDIAD) study. *J. Chem. Phys.* **1989**, *90*, 4604–4612.

(51) Surnev, S.; Vitali, L.; Ramsey, M.; Netzer, F.; Kresse, G.; Hafner, J. Growth and structure of ultrathin vanadium oxide layers on Pd (111). *Phys. Rev. B* **2000**, *61*, 13945.

(52) Tang, Z.; Wang, S.; Zhang, L.; Ding, D.; Chen, M.; Wan, H. Effects of O_2 pressure on the oxidation of VO_x/Pt (111). *Phys. Chem. Chem. Phys.* **2013**, *15*, 12124–12131.

TOC Graphic

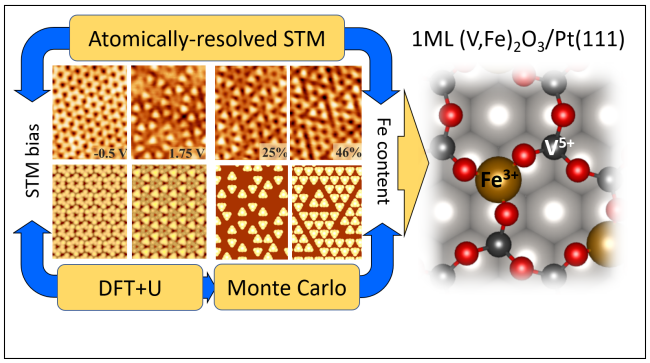
Atomically-resolved STM
1ML (V,Fe)2O3/Pt(111)
STM bias
-0.5 V
1.75 V
25%
46%
Fe content
V5+
Fe3+
DFT+U
Monte Carlo